The Monte Carlo Method: Versatility Unbounded In A Dynamic Computing World
Chattanooga, Tennessee, April 17–21, 2005, on CD-ROM, American Nuclear Society, LaGrange Park, IL (2005)

DOSIMETRIC IMPACT OF SCATTERED PHOTON SUBSOURCES WITHIN A MONTE CARLO PHOTON BEAM SOURCE MODEL FOR DIFFERENT INITIAL MEAN ELECTRON ENERGIES

Michael K. Fix, Paul J. Keall and Jeffrey V. Siebers
Department of Radiation Oncology
Virginia Commonwealth University, P.O. Box 980058, Richmond, VA 23298
mkfix@vcu.edu; pjkeall@vcu.edu; jvsiebers@vcu.edu

ABSTRACT

Widespread implementation of Monte Carlo (MC) codes suitable for patient dose calculation has been limited due to the lack of a general, accurate, and user-specific scalable source model of the accelerator radiation source. For histogram-based MC source models to have broad applicability, they require methods to scale to the user-specific accelerator output. This work investigates the dosimetric impact of changes in scattered photon subsources due to changes in the mean initial electron energy ($\overline{E}_e$) striking the bremsstrahlung target and determines what scaling of those subsources is required to match dose distributions generated with different $\overline{E}_e$. Tests were performed for 6-MV beams using $\overline{E}_e$=5, 6.2 and 7 MeV and for 18-MV beams using 17, 18, and 19 MeV. Phase–space data was transformed into histogram distributions for a previously developed MC source model. 3D dose distributions for a 10×10-cm^2 field in water were calculated using different subsource combinations. When scattered photon subsources associated with the 5-MeV simulation were used with the 7-MeV target subsource, <0.3% differences were found compared with using all the 7-MeV subsources. Differences were reduced to <0.2% when using the 6.2-MeV scattered subsources with the 7-MeV target subsource and were <0.1% when using either 17- or 18-MeV scatter subsources with the 19-MeV target subsource for 18-MV beams. These results indicate that apart from scaling the scattered subsource intensity, only the target subsource distributions need to be changed to adjust the source model to dosimetrically match accelerator outputs due to $\overline{E}_e$ changes.

Key Words: Monte Carlo simulation, source model tuning, photon energy distribution

1 INTRODUCTION

Given the availability of fast radiotherapy-specific Monte Carlo (MC) codes, the major limitation to the widespread implementation of MC dose calculations is the lack of a generalized source model of the linear accelerator radiation source. More precisely, a user with an arbitrary linear accelerator should be able to commission the source model so that the MC dose-calculation algorithm meets predefined accuracy requirements compared with measurements obtained prior to using the algorithm for patient dose calculation, e.g., 2% or 2 mm [1]. A promising approach for overcoming this limitation is to create a histogram-based source model from precalculated phase–space data (PSD) [2-6]. Such PSD can be generated by full MC simulations of the radiation transport through the accelerator head, usually through the part that is patient-independent. Thereby, the position, momentum, energy and charge are stored in a phase–space (PS) file for each particle traversing the plane in which the PSD is scored (PS-scoring plane). This PSD provides accurate particle distributions in the PS plane, thus the data

can be used to create a histogram-based source model, in which each subsource is characterized by a set of histograms [6]. By sampling the initial parameters of a particle from these histogram distributions, such a source model reconstructs the photon beam at the PS plane.

The drawback of histogram-based PSD models is that they generally require computation of the basis PSD to generate the histograms, which requires both local MC expertise and substantial time and effort. For histogram-based models to be broadly applicable, a general method needs to be developed to adjust the histogrammed subsources to match user-specific measurements, which does not require local MC expertise.

It has been shown that the photon beam for linear accelerators with slightly different output can be characterized by adjusting the parameters of the electron beam above the target [7-9]. A previous study investigated the impact of changing the energies and radial distributions of initial electrons striking a linear accelerator target on the photon-beam subsource distributions in an MC source model for 6- and 18-MV photon beams [10]. The results indicated that adjustments to the photon subsources can likely be limited to adjusting the target subsource in conjunction with scaling the relative intensities and energy spectra of the primary collimator (PC) and flattening filter (FF) subsources when the energies and radial distributions of the initial electron beams change. However, the variations in the energy spectra for the scattered photon subsources (PC and FF) are small, and the impact of these changes on dose distributions has not yet been studied.

The aim of this work is to investigate the dosimetric impact of the variations in the beam characteristics of the scattered photon subsources with a previously developed MC source model for 6- and 18-MV photon beams [6] and determine what scaling (if any) of those subsources is required to match dose distributions generated with different initial electron energies.

2 METHODS AND MATERIALS

In this section, the creation of the PSD for the various settings of the initial electron beam is described followed by an outline of the MC histogram-based source model and a detailed description of the dose calculations.

The general procedure used in this study is illustrated in Figure 1. PSD was calculated using different initial mean energies for the electrons striking the target, and histograms for each subsource were created from the PSD [6]. For each different mean electron energy, the relative contribution (weight) of each subsource was determined. Dose to a phantom was computed using the target subsource associated with the maximum electron energy and with the scattered photon subsources associated with each of the other energies simulated. The relative subsource weights were set to be equal to that for the maximum electron energy on the target. Dose in phantom for the various subsource combinations was compared using the pure maximum-electron energy subsources as a standard.

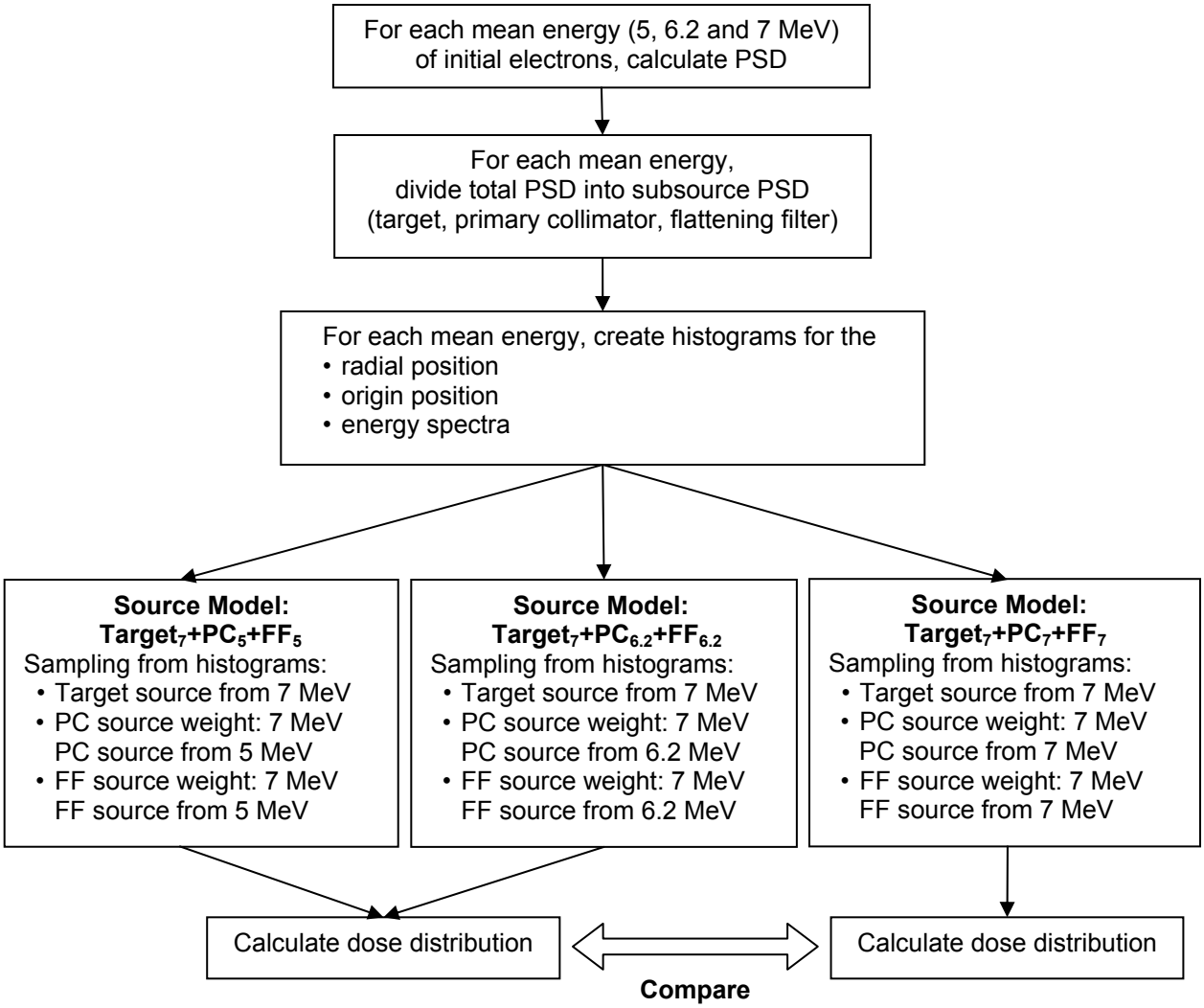

Figure 1. Illustration of the procedure. Phase–space data (PSD) were calculated for different mean energies of the initial electron beams (5, 6.2 and 7 MeV). Histograms for the source model were created, and dose distributions were calculated for different beam configurations using the same target subsource, but different scattered photon subsources, in order to evaluate their impact on the dose distributions. Finally, the calculated dose distributions were compared. For the 18-MV beam, substitute the mean electron energies 5, 6.2 and 7 MeV with 17, 18 and 19 MeV. FF: flattening filter; PC: primary collimator.

2.1 Phase-space data

BEAMnrc [11] was used to perform the MC simulations of the radiation transport of a Varian Clinac 21EX (Varian Oncology Systems, Palo Alto, CA 94304) for 6- and 18-MV photon beams. Simulations were initiated with electrons impinging the target. Particles including secondaries were transported through the target, PC, vacuum window, FF, monitor chamber, and field light mirror with intervening air below the vacuum window. The PS-scoring plane was located perpendicularly to the beam axis and directly above the secondary collimator jaws. The

initial electron beam is characterized by the mean electron energy $\overline{E}_e$, the normally distributed electron energy spread σ_E, and the normally distributed radial intensity σ_r. According to a previously performed sensitivity study [10], the largest changes in the beam characteristics for the scattered photon subsources appear in the energy spectrum when the parameter $\overline{E}_e$ of the initial electron beam is changed. Consequently, and in agreement to a previous publication [6], σ_E was set to 1.28% of the mean energy, which corresponds with a full width half maximum (FWHM) of 3%, and σ_r was set to 0.96 mm, which corresponds with a FWHM of 2.27 mm, for the 6-MV beam. For the 18-MV beam, σ_E was again set at 1.28%, whereas σ_r was set to 0.64 mm. For the mean electron energy $\overline{E}_e$, the following values were used: 5, 6.2 and 7 MeV for the 6-MV beam and 17, 18 and 19 MeV for the 18-MV beam, covering the range used for PSD calculations at several research institutions [3, 4, 7-9, 12].

For all of the MC simulations generating the PSD, the threshold energies for electron and photon transport, ECUT and PCUT, were set to 0.70 and 0.010 MeV, respectively, except in the target for the 18-MV beam. In this case, the value of PCUT was increased to 0.15 MeV, which had been previously shown to have a negligible impact on the PSD [8]. The discrete electron- and photon-creation thresholds, AE and AP, were set to 0.70 and 0.010 MeV, respectively. The "uniform bremsstrahlung splitting" variance reduction technique was applied with a bremsstrahlung splitting number of 20. The splitting number is not applied to higher-order bremsstrahlung and annihilation photons. For the 6- and 18-MV beams, at least 100×10^6 and 20×10^6 histories, respectively, were simulated, leading to at least 106×10^6 (6-MV) and 95×10^6 (18-MV) particles in the PSD files.

The total PSD at a given z coordinate stored the following information for each particle P traversing the PS-scoring plane:

$$P = [x, y, u, v, E, q, weight, LATCH] \tag{1}$$

where x and y are the position coordinates of the particle; u and v are the direction cosines in the x and y directions, respectively; E is the energy; q is the charge; *weight* is the particle statistical weight; and *LATCH* is a tag that records where particles originated or interacted previously. The total PSD was separated into PSD files for the target, the PC and the FF, based on the location of the last interaction of the photons determined by the LATCH variable. The PSD from these three photon subsources included over 99.5% of all photons scored in the total PSD file. The remaining 0.5% of the photons was excluded from this study, since these photons had had their last interaction in air or in one of the other head components (ionization chamber, mirror, etc.).

2.2 Source model

Because the source model used in this study is described in detail in Reference [6], this section only briefly reviews the model.

Within the source model, the dimensionality of the parameter space described by Equation 1 is simplified, since all particles used to create the histograms have equal statistical weight, and charged particles are considered as a separate subsource. This reduces the PSD to a sequence of multidimensional functions $F_i(x,y,u,v,E)$, where i denotes the i^{th} subsource. The histogram

representation of the source model used takes advantage of the radial symmetry of the beam at the PS-scoring plane and is of the form

$$F_i(x, y, u, v, E) = f_i(r_s, \varphi_s, r_o(r_s), \varphi_o(r_s, r_o)) g_i(E(r_s, r_o)), \quad (2)$$

where x_s, y_s and $r_s = (x_s^2 + y_s^2)^{1/2}$ are the coordinates of the particle in the sampling plane, r_o and φ_o are the coordinates in the origin plane, and E is the particle's energy. The sampling plane is typically the isocenter plane, and the origin plane is located coincidently with the exit surface of the i^{th} subsource component in the accelerator head perpendicular to the beam axis. Thus, the function f_i determines the position and direction within the PS-scoring plane from a point in the sampling and origin plane, and g_i is used to determine the particle's energy. Within the source model, the functions f_i and g_i are represented by a set of histograms that were created by projecting the particle coordinates from the PS-scoring plane to the sampling plane and the origin plane, respectively, using ray-tracing techniques. Hence, g_i and f_i describe the beam characteristics of the subsource, and sampling from the histogram distributions reproduces the PSD.

2.3 Source configurations and dose calculations

Different linear combinations of the above-defined subsources were used to compute the dose to a water phantom. In the first test case, the scattered photon subsources obtained by the lowest mean electron energy (5 MeV) were combined with the target subsource from the highest mean electron energy (7 MeV). The relative subsource weights were set as equal to those associated with the mean electron energy used for the target subsource. This beam configuration is referred to as: $target_7+PC_5+FF_5$. Dose calculations with this beam configuration were compared with those using a beam configuration consisting of the target and scattered subsource characteristics associated with the 7 MeV simulation, denoted as $target_7+PC_7+FF_7$. The corresponding test case for the 18-MV beam used 17 and 19 MeV instead of 5 and 7 MeV, respectively. Consequently, the notations for these beam configurations are $target_{19}+PC_{17}+FF_{17}$ and $target_{19}+PC_{19}+FF_{19}$. These comparisons evaluate the maximum impact on dose distributions by scattered subsources from different initial mean electron energies $\overline{E}_e$.

In addition to testing the extreme situation, a more realistic test case was defined by comparing the beam configurations $target_7+PC_7+FF_7$ and $target_{19}+PC_{19}+FF_{19}$ from above with those taking the scattered subsource characteristic from the 6.2-MeV (18-MeV) simulations, but again using the relative subsource weights and the target subsource from the 7-MeV (19-MeV) simulation. In other words, the subsources from the expected mean electron energy were used with the maximum likely mean electron energy in this test case. Consequently, these test cases are referred to as $target_7+PC_{6.2}+FF_{6.2}$ and $target_{19}+PC_{18}+FF_{18}$. In Figure 1, the procedures and comparisons are illustrated for the 6-MV beam.

The dose calculations were executed in two stages. In the first stage, particles sampled from the source model were transported through the secondary collimator and intervening air using BEAMnrc, which, in turn, generated a PS file immediately above the phantom surface. In the second stage, the BEAMnrc PS file was used as an input for DOSXYZnrc [11] to perform the dose calculations within a water phantom. Dose distributions with the phantom at a source-to-surface distance (SSD) of 100 cm were calculated and compared for a field size of 10×10 cm^2.

The dose voxel size was 0.4×0.4×0.4 cm^3, and the statistical uncertainty of each dose calculation was less than 1% at a depth of D_{max}.

The resulting 3D dose distributions were normalized to the same integral dose for the depth dose curve and compared in terms of dose difference. Such a normalization is reasonable since a given user would perform such a normalization when determining the conversion factor between monitor units and the number of source particles during beam commissioning [13]. Nonetheless, it will be shown that these normalizations themselves were small.

Dose distributions D_1 and D_2, where D_1 is the reference distribution and D_2 is the test distribution, were compared using the difference $D_1 - D_2$ divided by the maximum (D_1). To reduce the effects of statistical uncertainty in the plots, in the depth doses and in the dose differences shown in the figures, the dose values were averaged over three voxels in both lateral directions so that the effective voxel size for the depth–dose plots was 1.2×0.4×1.2 cm^3. Similarly, the lateral profiles shown were averaged along three voxels in the depth considered and the orthogonal direction.

3 RESULTS AND DISCUSSION

Table I shows the relative weights of the photon subsources within the source model for various mean energies of the initial electron beam.

Table I. Relative subsource weights within the source model for various initial mean energies of the electron beam. The contribution of each subsource as fraction of the dose at dose maximum is given in parenthesis.

Mean electron energy	Target	Primary collimator	Flatteningfilter
5 MeV	0.883 (93.7%)	0.040 (2.6%)	0.077 (3.7%)
6.2 MeV	0.8805 (94.0%)	0.0415 (2.5%)	0.078 (3.5%)
7 MeV	0.8772 (94.3%)	0.0428 (2.4%)	0.080 (3.3%)
17 MeV	0.845 (92.5%)	0.0408 (1.4%)	0.1142 (6.1%)
18 MeV	0.8432 (92.6%)	0.041 (1.3%)	0.1158 (6.1%)
19 MeV	0.841 (92.8%)	0.0411 (1.2%)	0.1179 (6.0%)

With increasing mean electron energies $\overline{E}_e$, the relative weight of the target subsource decreases and, consequently, the relative weight of the scattered subsources increases. The ratio of the subsource weight for the FF to the one for the target changed by about 4.5% for the 6-MV beam, when the mean electron energy was changed from 5 to 7 MeV. For the 18-MV beam, this ratio increased by about 3.7% when the mean electron energy was changed from 17 to 18 MeV. The ratio of the PC's weight to the target weight varied by about 7.7% (6 MV) and 1.2% (18 MV) – within the range of the mean electron energy used.

Figure 2(a) and (b) compare the depth doses and lateral dose profiles for the beam configurations *target$_7$+PC$_5$+FF$_5$* and *target$_7$+PC$_7$+FF$_7$*. The dose profiles are plotted at a depth of dose maximum (1.5 cm), 5, 10, and 20 cm in water.

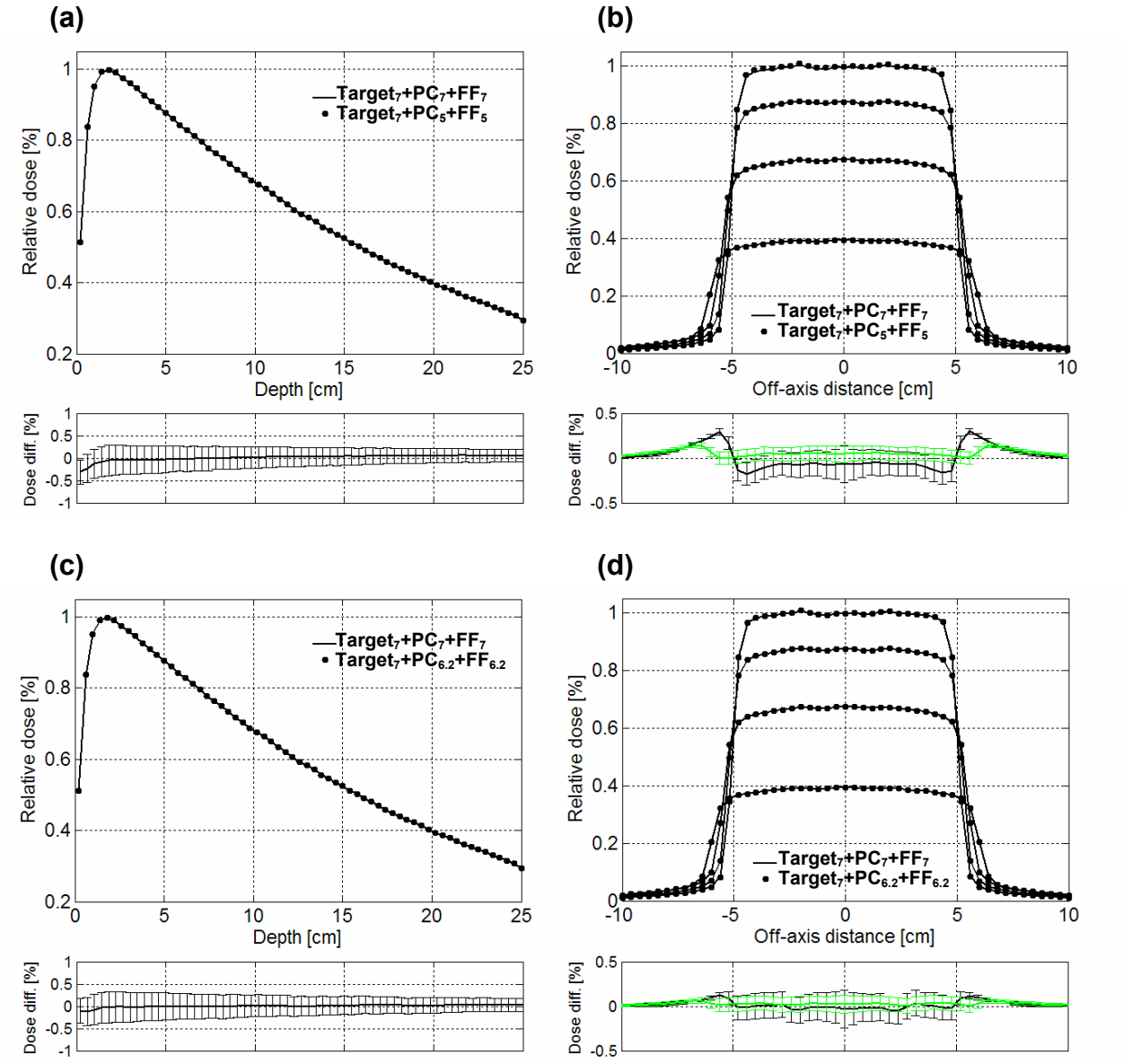

Figure 2. Depth dose distributions and lateral dose profile comparisons for beam configurations of the 6-MV beam. (a) Depth doses for the beam configurations target$_7$+PC$_7$+FF$_7$ (notation described in 2.3) and target$_7$+PC$_5$+PC$_5$, together with a dose difference plot. (b) Same as (a) for the dose profiles at a depth of dose maximum, 5, 10 and 20 cm in water; dose differences plotted at a depth of dose maximum (black line) and 20 cm (green line). (c) Depth doses for the beam configurations target$_7$+PC$_7$+FF$_7$ and target$_7$+PC$_{6.2}$+PC$_{6.2}$, together with a dose difference plot. (d) Same as (c) for the dose profiles at a depth of dose maximum, 5, 10 and 20 cm in water; dose differences plotted at a depth of dose maximum (black line) and 20 cm (green line). PC: Primary collimator; FF: Flattening filter.

Together with the dose values, dose difference plots are shown for the depth doses [below Figure 2(a)] and the lateral dose profiles at two depths [below Figure 2(b)]: one at a depth of dose maximum (black solid line) and one at a depth of 20 cm in water (green solid line). Minor dose differences (<0.3%) occurred at shallow depths for the depth doses and at the beam edge for the lateral dose profiles. The softer energy distribution for PC_5 and FF_5, compared with PC_7 and FF_7 [10], results in the dose maximum being closer to the surface for the $target_7+PC_5+FF_5$ and an increased dose falloff beyond the dose maximum. However, these deviations are well within the statistical uncertainty of a typical MC computation. Furthermore, the lateral scatter of these subsources increased.

Dose distribution comparisons for the second, more realistic scaling test case – using the beam configurations $target_7+PC_{6.2}+FF_{6.2}$ and $target_7+PC_7+FF_7$ – are depicted in Figure 2(c) and (d). The dose differences in this test case were less than 0.2%. The normalization applied to equate the integral doses for the test cases are summarized in Table II. Although the normalization correction for the $target_7+PC_5+FF_5$ simulation is 0.8%, it is inconsequential since this normalization would automatically occur when a user calibrated the source model to match the accelerator monitor unit output.

Table II. Normalization factors for the different beam configurations used for the 6-MV beam.

Beam configuration	Normalization factor
$\mathbf{Target_7+PC_5+FF_5}$	1.008
$\mathbf{Target_7+PC_{6.2}+FF_{6.2}}$	1.002
$\mathbf{Target_7+PC_7+FF_7}$	1.000

FF: flattening filter; PC: primary collimator.

The results for the 18-MV beam show the same trends, though of lower magnitudes, as those for the 6-MV beam. Figure 3(a) and (b) depict the depth dose distributions and the lateral dose profiles at a depth of dose maximum (3 cm), 5, 10, and 20 cm in water for the beam configurations $target_{19}+PC_{17}+FF_{17}$ and $target_{19}+PC_{19}+FF_{19}$. Below the plots for the dose distributions are the dose differences for the depth dose [Figure 3(a)] and for the dose profiles [Figure 3(b)] at two different depths: one at a depth of dose maximum (black solid line) and one at a depth of 20 cm (green solid line) in water. Almost all differences were smaller than the statistical uncertainty.

Figure 3(c) and (d) compare the dose distributions for the beam configurations $target_{19}+PC_{18}+FF_{18}$ and $target_{19}+PC_{19}+FF_{19}$. In this comparison, all dose differences were within the statistical uncertainties of the dose calculations. Additionally, the normalization factors were all very close to 1 and are reported in Table III. The decreased dosimetric impact for the 18-MV beam, compared with the 6-MV beam for the different beam configurations, is in agreement with a previous study [10] in which it was shown that for the 18-MV beam, the sensitivity of the beam characteristics on the scattered subsource is lower in magnitude than for a

6-MV beam for 1-MeV changes in the mean electron energy $\overline{E}_e$. These results demonstrate that the beam characteristics of the scattered subsources are nearly independent of the mean energy of the initial electron beam.

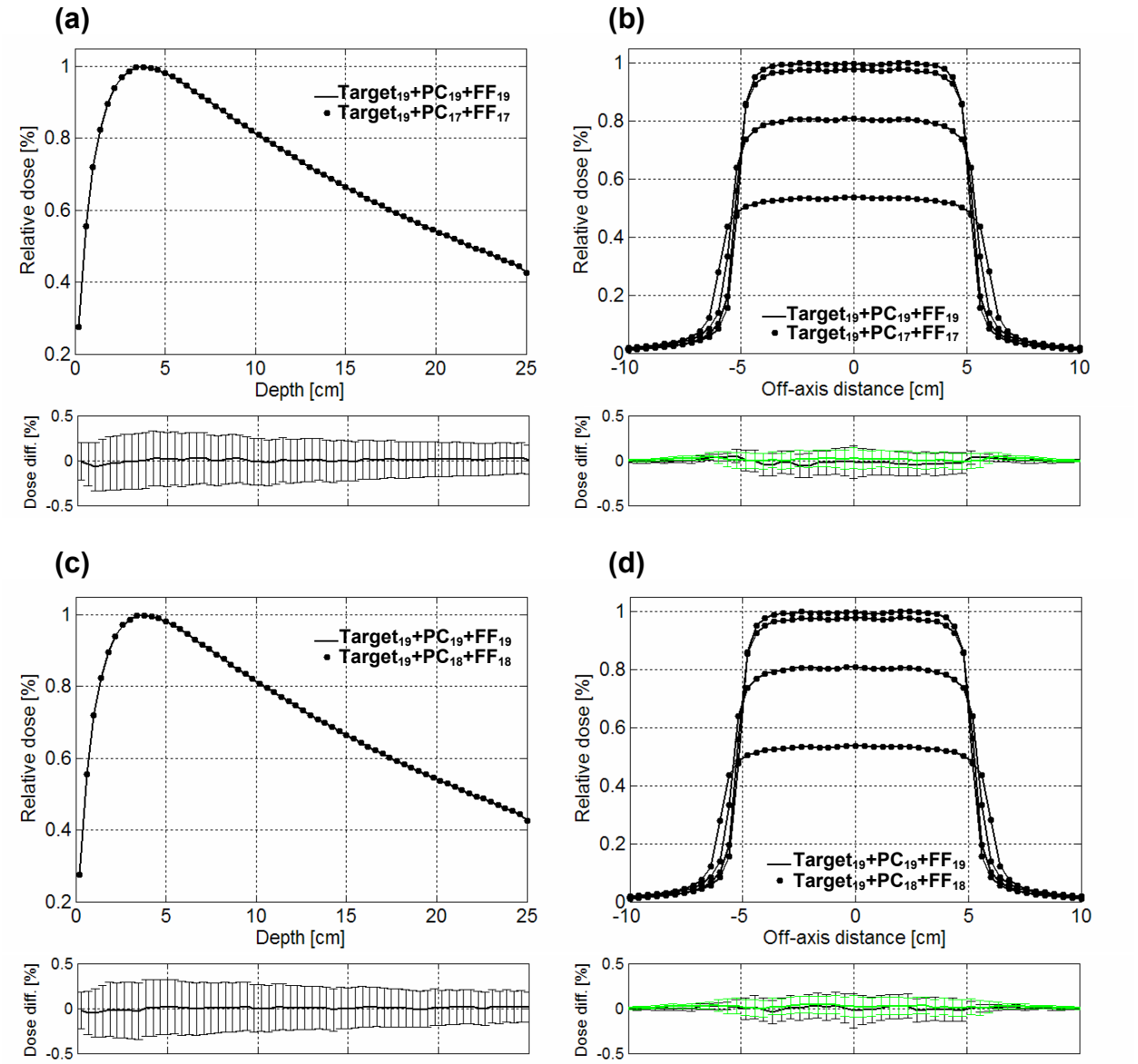

Figure 3. Depth dose distributions and lateral dose profiles comparisons for beam configurations of the 18-MV beam. (a) Depth doses for the beam configurations target$_{19}$+PC$_{19}$+FF$_{19}$ (notation described in 2.3) and target$_{19}$+PC$_{17}$+PC$_{17}$, together with a dose difference plot. (b) Same as (a) for the dose profiles at a depth of dose maximum, 5, 10 and 20 cm in water; dose differences plotted at a depth of dose maximum (black line) and 20 cm (green line). (c) Depth doses for the beam configurations target$_{19}$+PC$_{17}$+FF$_{17}$ and target$_{19}$+PC$_{18}$+PC$_{18}$, together with a dose difference plot. (d) Same as (c) for the dose profiles at a depth of dose maximum, 5, 10 and 20 cm in water; dose differences plotted at a depth of dose maximum (black line) and 20 cm (green line). PC: Primary collimator; FF: Flattening filter.

Table III. Normalization factors for the different beam configurations used for the 18-MV beam.

Beam configuration	Normalization factor
$\mathbf{Target_{19}+PC_{17}+FF_{17}}$	1.0020
$\mathbf{Target_{19}+PC_{18}+FF_{18}}$	1.0009
$\mathbf{Target_{19}+PC_{19}+FF_{19}}$	1.0000

FF: flattening filter; PC: primary collimator.

4 CONCLUSIONS

General-use histogram-based MC source models require a method to adjust the individual subsources in the source model to match user-specific beam characteristics based upon measured dose distributions. A previous study indicates that source model adjustments can likely be limited to adjusting the target subsource in conjunction with scaling the relative subsource weights and energy spectra of the scattered photon subsources when the initial electron-beam parameters change [10]. Whereas the previous study investigated the energy and radial distributions of the subsources, this study evaluated its dosimetric impact for the scattered photon subsources.

In this study, we found that using scattered subsources for photon beams determined with a different initial mean electron energy than that for the target but scaled according to their relative weights (Table I) at the target energy resulted in <0.3% dosimetric error for the 6-MV beam for the beam tested. For the 18-MV beam, the error was less than 0.1%. These dosimetric errors were reduced when the scattered subsources were taken from the expected mean electron energy, compared with scaling from the minimum energy tested to the maximum. Hence, apart from scaling the relative weights for the scattered subsources in a PS model, only the target subsource needs to be changed in order to adjust the source model to match data from an accelerator tuned to a different energy. This greatly simplifies the adjustments required for histogrammed subsources to match user-specific accelerator output and, with the addition of scaling for the target subsource, will allow for general and widespread use of accurate histogram-based source models for MC-based radiation-therapy dose calculations.

5 ACKNOWLEDGMENTS

The authors wish to thank Devon Murphy for improving the clarity of this article due to her careful review. Varian Medical Systems provided us with the engineering diagrams and material specifications required for the modeling of the linear accelerators. We acknowledge the financial support of Philips Medical Systems, ACS Grant IRG-73-001-28 and NIH Grant 1R01CA098524.

6 REFERENCES

1. J. Van Dyk, R. B. Barnett, J. E. Cygler and P. C. Shragge, "Commissioning and quality assurance of treatment planning computers," *Int J Radiat Oncol Biol Phys*, **26**, pp. 261-273 (1993).
2. C. M. Ma, B. A. Faddegon, D. W. Rogers and T. R. Mackie, "Accurate characterization of Monte Carlo calculated electron beams for radiotherapy," *Med Phys*, **24**, pp. 401-416 (1997).
3. A. E. Schach von Wittenau, L. J. Cox, P. M. Bergstrom, Jr., W. P. Chandler, C. L. Hartmann Siantar and R. Mohan, "Correlated histogram representation of Monte Carlo derived medical accelerator photon-output phase space," *Med Phys*, **26**, pp. 1196-1211 (1999).
4. J. Deng, S. B. Jiang, A. Kapur, J. Li, T. Pawlicki and C. M. Ma, "Photon beam characterization and modelling for Monte Carlo treatment planning," *Phys Med Biol*, **45**, pp. 411-427 (2000).
5. M. K. Fix, M. Stampanoni, P. Manser, E. J. Born, R. Mini and P. Ruegsegger, "A multiple source model for 6 MV photon beam dose calculations using Monte Carlo," *Phys Med Biol*, **46**, pp. 1407-1427 (2001).
6. M. K. Fix, P. J. Keall, K. Dawson and J. V. Siebers, "Monte Carlo source model for photon beam radiotherapy: photon source characteristics," *Med Phys*, **31**, pp. 3106-3121 (2004).
7. D. Sheikh-Bagheri and D. W. O. Rogers, "Sensitivity of megavoltage photon beam Monte Carlo simulations to electron beam and other parameters," *Med Phys*, **29**, pp. 379-390 (2002).
8. P. J. Keall, J. V. Siebers, B. Libby and R. Mohan, "Determining the incident electron fluence for Monte Carlo-based photon treatment planning using a standard measured data set," *Med Phys*, **30**, pp. 574-582 (2003).
9. G. X. Ding, "Energy spectra, angular spread, fluence profiles and dose distributions of 6 and 18 MV photon beams: results of monte carlo simulations for a varian 2100EX accelerator," *Phys Med Biol*, **47**, pp. 1025-1046 (2002).
10. M. K. Fix, P. J. Keall and J. V. Siebers, "Photon-beam subsource sensitivity to the initial electron-beam parameters," *submitted to Medical Physics*, (2004).
11. D. W. O. Rogers, B. A. Faddegon, G. X. Ding, C. M. Ma, J. We and T. R. Mackie, "BEAM: a Monte Carlo code to simulate radiotherapy treatment units," *Med Phys*, **22**, pp. 503-524 (1995).
12. C. L. Hartmann Siantar, R. S. Walling, T. P. Daly, B. Faddegon, N. Albright, P. Bergstrom, A. F. Bielajew, C. Chuang, D. Garrett, R. K. House, D. Knapp, D. J. Wieczorek and L. J. Verhey, "Description and dosimetric verification of the PEREGRINE Monte Carlo dose calculation system for photon beams incident on a water phantom," *Med Phys*, **28**, pp. 1322-1337 (2001).
13. J. V. Siebers, P. J. Keall, B. Libby and R. Mohan, "Comparison of EGS4 and MCNP4b Monte Carlo codes for generation of photon phase space distributions for a Varian 2100C," *Phys Med Biol*, **44**, pp. 3009-3026 (1999).